High-Frequency Aeroacoustic Source Mechanisms of a Structured Porous Coated Cylinder

Original
High-Frequency Aeroacoustic Source Mechanisms of a Structured Porous Coated Cylinder / Arcondoulis, Elias; Zamponi, Riccardo; Alagoz, Iris; Avallone, Francesco; Paruchuri, Chaitanya. - (2024). (30th AIAA/CEAS Aeroacoustics Conference (2024) Rome (ITA) June 4-7, 2024) [10.2514/6.2024-3342].

Publisher:
American Institute of Aeronautics and Astronautics

Published
DOI:10.2514/6.2024-3342

High-frequency aeroacoustic source mechanisms of a structured porous coated cylinder

Elias J. G. Arcondoulis*
University of Bristol, BS8 1TR Bristol, United Kingdom

Riccardo Zamponi†
Delft University of Technology, 2629HS Delft, The Netherlands
von Karman Institute for Fluid Dynamics, B-1640 Sint-Genesius-Rode, Belgium

İris Alagöz‡
von Karman Institute for Fluid Dynamics, B-1640 Sint-Genesius-Rode, Belgium

Francesco Avallone§
Politecnico di Torino, 10129 Torino, Italy

Chaitanya Paruchuri¶
University of Southampton, SO17 1BJ Highfield, United Kingdom

The application of a porous coating to a bluff body, such as a cylinder, is an efficient passive flow control method and has applications in wind, aerospace, and civil engineering. Despite its effectiveness in reducing vortex-shedding processes and the associated noise-generating mechanisms, there exists a trade-off in terms of the generation of higher frequency noise. Such acoustic emissions can be irritating to the human ear and thereby diminish some of the benefits of porous media as a form of passive flow and noise control. To date, explanations of the mechanisms responsible for high-frequency noise generation of a porous coated cylinder (PCC) are qualitative, and there is no clear consensus. In this paper, it is hypothesized that the high-frequency noise is caused by local vortex shedding around the structural members of the pores that comprise the porous media on the cylinder windward side. To investigate this claim, a mathematical model is derived based on the premise that a porous cylinder potential flow model accurately captures the total velocity at the outer diameter of a PCC. The acoustic shedding frequencies are assumed to be related to the Strouhal number relationship, and the acoustic intensity is assumed to be consistent with Curle's theory, where acoustic intensity scales with the sixth power of flow velocity and the characteristic length squared. A lattice-Boltzmann method simulation of a simplified structured PCC, following a previously published design, is used to test the analytical model, yielding excellent agreement with the mathematical model in terms of acoustic intensity and frequency range.

I. Introduction

Vortex shedding often takes place in the wake of a bluff body and potentially generates tonal noise linked to the body's characteristic width. This is referred to as the Aeolian tone [1–3] and can be problematic for the design of aircraft landing gear [4, 5], high-speed train pantographs [6, 7] and chimney stacks [8], which can be approximated as a cylinder, to some degree. The coating of open-cell porous materials around a cylinder (porous coated cylinder: PCC) can act as an effective form of passive flow and noise control, as demonstrated by many studies in the last 10-15 years [9]. Recent investigations have shown that porous media can entrain flow, modify the wake region, reduce the vortex shedding tone amplitude, and shift its frequency based on the trajectory of the shear layer [10]. In this regard, the

---

*Lecturer, School of Civil, Aerospace and Design Engineering, elias.arcondoulis@bristol.ac.uk, AIAA Senior Member

†Guest Researcher and Lecturer, Department of Flow Physics and Technology, r.zamponi@tudelft.nl, AIAA Member

‡Short-training-programme student, Department of Environmental and Applied Fluid Dynamics, iris.alagoz@metu.edu.tr

§Full Professor, Department of Mechanical and Aerospace Engineering, francesco.avallone@polito.it, AIAA Member

¶Associate Professor, Institute of Sound and Vibration Research, C.C.Paruchuri@soton.ac.uk, AIAA Member

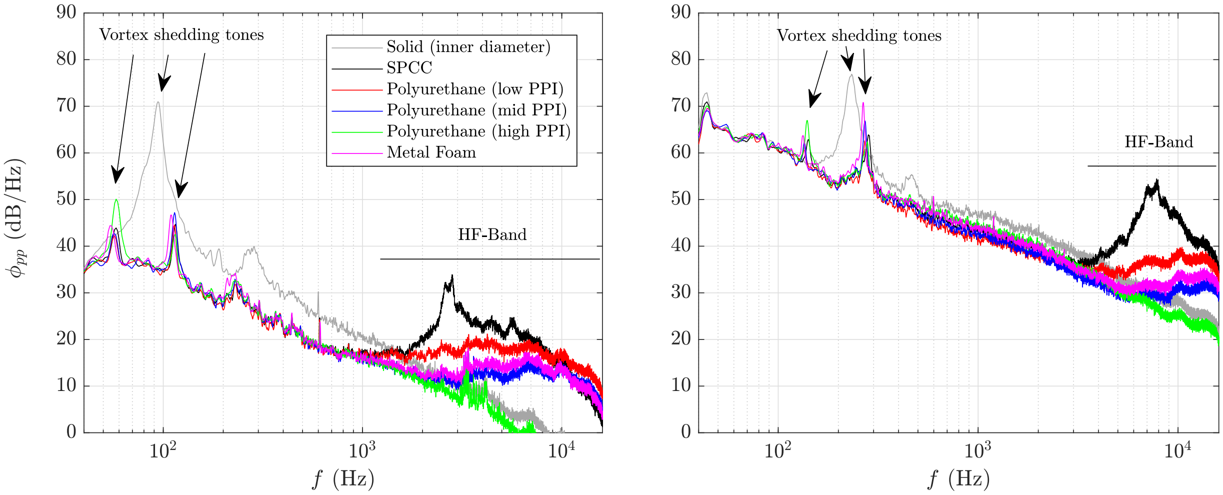

Fig. 1 Vortex shedding tones and HF-Band of several PCCs with an outer diameter of 60 mm **and a solid cylinder of diameter** 40 mm **(same diameter as the inner diameter of the PCCs), subject to freestream velocities (a)** $U_0 = 20\,\mathrm{m\,s^{-1}}$ **(outer diameter Reynolds number,** $Re_D \approx 8 \times 10^4$ **and (b)** $50\,\mathrm{m\,s^{-1}}$ ($Re_D \approx 2 \times 10^5$)**. Data are obtained from Refs. [12] and [13].**

downstream displacement of the vortex-shedding onset and the decrease in the strength of the quadrupolar sources in the wake represent the dominant noise-mitigation mechanisms [11].

Typically, randomized open-cell porous media, such as porous polyurethane and metal foam, are used to coat cylinders for passive flow and noise control, with an open-to-solid porosity ranging from 75% to 95% and pores per inch (PPI) ranging from 10 PPI to 30 PPI [12, 13] for cylinders with diameters between 30 mm and 60 mm. More recently, Arcondoulis et al. [12] designed a Structured Porous Coated Cylinder (SPCC) to quantify the flow field within the porous layers of a PCC, numerically and experimentally. The SPCC has elliptical-shaped pores that are regularly spaced along the span and around the circumference, which allows independent control of porosity and PPI that is not possible with randomized porous media. The ability to 3-D print an SPCC using transparent materials (such as ultraviolet epoxy resins), in conjunction with its regularly spaced pore structure and LOS, unlocks the potential to quantify the flow field within the porous layers using methods such as tomographic particle image velocimetry (TPIV) [10]. To illustrate the passive noise control properties of PPCs, the acoustic far-field spectra, ϕ_{pp} (dB Hz^{-1}), of several PCCs and an SPCC are presented in Fig. 1. The vortex shedding peak of the PCCs and SPCC are more narrowband than the bare cylinder peak, which is also observed by others [11, 14–18]. According to Geyer [15], PCCs have much longer spanwise correlation lengths (greater than 8 outer diameters) relative to a solid cylinder (approximately 2–3 diameters [19]). As a result, solid cylinders shed vortices with slightly different length scales and thus emit noise over a slightly wider frequency range than PCCs. One clear disadvantage, however, of PCCs, and especially the SPCC, is that an acoustic high-frequency band contribution is also observed (referred to here as the HF-Band) [11, 12, 17].

Little is understood about this widely published high-frequency band, and it is often speculated that the noise is generated by acoustic resonances within the porous layer, surface roughness, and/or small-scale vortex shedding processes about each individual pore structural member. In this study, it is assumed that the latter is the primary noise-generating mechanism. It should be noted that the HF-Band varies based on modifications to the internal porous structure [17], implying that all porous structures from the outer to inner diameter may influence the generation of the HF-Band.

To test this hypothesis, a mathematical model is derived that aims to predict the HF-Band of PCCs. A 3-D numerical Lattice-Boltzmann Method (LBM) simulation of a simplified pore-scale model was conducted, which follows the PCC design of Wen et al. [20] and is presented in this work. This model uses an array of small solid cylinders around a larger solid cylinder to mimic the salient flow features of structured porous media. As shown in the acoustic and flow field analysis of Wen et al. [20], good agreement is observed between their simplified pore-scale model and experimental results of the 3-D SPCC by Arcondoulis et al. [12]. Due to the relative simplicity of the simplified 2-D pore-scale model, as compared to the 3-D SPCC, it was chosen as an ideal candidate to test the prediction capability of the derived mathematical model.

An analytical framework to explain the HF-band is proposed in this paper. It is assumed that each structural member can be treated as a bluff body that is subject to a local flow field. By knowing the dimension of the structural member (i.e., the characteristic length scale) and the velocity amplitude to which it is subject to, a sound source is assumed to be generated at each location on the outer porous surface of the PCC. The frequency of this sound can be computed using the Strouhal relationship, and its acoustic power can be estimated using Curle's formulation of a bluff body placed in a uniform flow [21]. An initial estimate of the far-field noise is derived using the local flow field at the PCC outer diameter using a potential flow model of a wholly porous cylinder [22] that is shown to have excellent agreement with experimentally obtained flow field results at the windward side of the SPCC near the outer diameter in the flow stagnation region. The use of the potential flow model allows for direct manipulation and substitution into Strouhal's equation and Curle's formulation to make analytical estimates of the frequency response function of the simplified pore-scale model and the total acoustic power output. This model is tested using simulated data total velocity obtained from an LBM simulation of a simplified SPCC model that is further validated via numerical acoustic beamforming.

The document is structured as follows. The theoretical framework behind the formulation of the presented model, the numerical methodology for computing the flow past the simplified SPCC, and the description of the numerical beamforming algorithm are outlined in Section II. Section III reports and discusses the main results, whereas Section V draws the concluding remarks.

II. Methodology

A. Underlying theory & small-scale vortex shedding hypothesis

The methodology of this study revolves around the following hypothesis: the HF-Band is caused by small-scale vortex shedding about the pore structural members on the SPCC windward surface. It is assumed that the vast majority of the recorded high-frequency contributions, due to vortex shedding processes, are generated at the windward region, within ±90° of the flow direction, which is supported by acoustic beamforming results [11, 23, 24] and by investigating a range of SPCC permutations with varying leeward and windward porosity [25]. Furthermore, it is initially assumed that only the outermost porous surface contributes to the high-frequency far-field spectra, as pores closer to the inner diameter experience significantly lower velocities as quantified via a TPIV experiment in a recent publication by Arcondoulis et al. [10]. The building block of this model commences simply from the Strouhal number, St, relationship

$$St = \frac{f\varphi}{u}, \tag{1}$$

where f is the vortex shedding frequency, φ is the characteristic length scale (such as a cylinder diameter), and u is the velocity amplitude to which the bluff body is subject. If the velocity field and characteristic length scale at every point on the outer surface of the SPCC is known, the Strouhal number relationship can be rearranged and act as a frequency-response function, $\boldsymbol{\Omega} = \Omega(r, \theta, z)$

$$\Omega(r, \theta, z) = St\frac{u(r, \theta, z)}{\varphi(r, \theta, z)}, \tag{2}$$

where r, θ, and z are the cylindrical coordinates of the bodies that produce vortex shedding. To quantify the far-field acoustic spectra, the acoustic intensity, I, of a body subject to a flow field by Curle [21] is estimated via

$$I(r, \theta, z) \sim \frac{\rho_0}{c_0^3} u^6(r,\ \theta,\ z)\varphi^2(r,\ \theta,\ z), \tag{3}$$

where ρ_0 is the fluid density and c_0 is the speed of sound. The frequency associated with this acoustic intensity is $\boldsymbol{\Omega}$. The total acoustic intensity for the entire HF-Band can, therefore, be calculated as

$$I_T = \iiint I(r, \theta, z)\, \mathrm{d}r\, \mathrm{d}\theta\, \mathrm{d}z. \tag{4}$$

By assuming that (i) the HF-Band is generated on the windward surface only and (ii) the flow field about the streamwise axis is symmetric on the windward side, the total acoustic intensity can be calculated using a windward quadrant of the cylinder of a portion of the cylinder span across z via

$$I_T \sim 2 \int_z \int_{\theta=0}^{\pi/2} \int_{r=d/2}^{D/2} I(r,\theta,z)\, \mathrm{d}r\, \mathrm{d}\theta\, \mathrm{d}z, \tag{5}$$

and substituting Eq. (3) into Eq. (5) yields

$$I_T \sim \frac{2\rho_0}{c_0^3} \int_z \int_{\theta=0}^{\pi/2} \int_{r=d/2}^{D/2} u^6(r,\theta,z)\varphi^2(r,\theta,z)\, \mathrm{d}r\, \mathrm{d}\theta\, \mathrm{d}z. \tag{6}$$

B. Structured porous coated cylinder design

An SPCC design is needed to test the small-scale vortex shedding hypothesis analytically and also via numerical simulation. As mentioned in Section I, the coated-cylinder configuration considered in the present study is from the work of Wen et al. [20], precisely the SRS98 case, which is characterized by an overall porous-medium porosity of 98 % and proved to be the most effective in mitigating the related flow-induced noise. The structured coating is modeled by four layers of small cylinders with diameters d_1 (for the innermost layer) to d_4 (for the outermost layer) wrapped around a bare cylinder of diameter $d = 40$ mm. The dimensions are $d_1 = 0.321$ mm, $d_2 = 0.350$ mm, $d_3 = 0.382$ mm, and $d_4 = 0.417$ mm. Note that the diameters of the small cylinders are related via $d_{n+1}/d_n = 1.09$ for $n = 1$ to 3. In the circumferential direction, the small cylinders are separated by an angle of 5°, resulting in a total number of 72 bodies in each layer, as depicted in Fig. 2. It should be noted that this SPCC design is especially attractive for testing the small-scale vortex shedding hypothesis, as each small cylinder responsible for the HF-Band has a simple characteristic length, being its diameter, d_n. The four layers are fit within a thickness h such that $h/d = 0.25$. As a result, the overall outer diameter of the porous coating can be estimated as $d + 2h = 1.5\,d$. The porous layer thickness to solid inner cylinder diameter ratio is 0.25, which is a commonly studied and highly effective ratio for passive flow and noise control of PCCs [26].

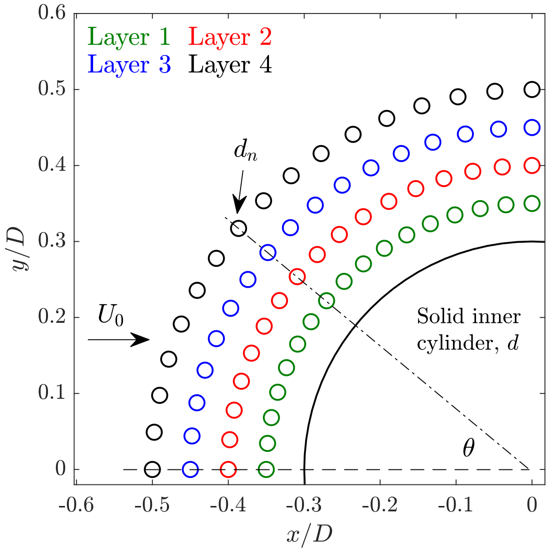

Fig. 2 Schematic diagram of the two-dimensional cylinder array case. The porous media is comprised of small cylinders with diameter, d_n, arranged in four layers (layer numbering increases with radial distance), spaced apart by $\Delta\theta = 5°$ and subject to freestream velocity U_0.

C. Numerical simulation

1. Flow solver

The flow field around the coated cylinder addressed in this paper has been computed using the commercial software 3DS Simulia PowerFLOW 6-2021. LBM equations, which compute the advection and collision of fluid particles using a statistical gas kinetic model, are at the base of the numerical technique. The discretization has been performed using 19 discrete velocities in three dimensions (D3Q19), using a third-order truncation of the Chapman-Enskog expansion [27]. The explicit time integration and collision model based on Bhatnagar-Gross-Krook (BGK) [28] are used. This model introduces a relaxation of the particle distribution function towards that of Maxwell-Boltzmann, describing gas particles at rest. The flow variables are calculated by integrating the particle distribution functions over the 19 discrete state directions. Turbulent fluctuations are modeled by extending the LBM to include an effective turbulent relaxation time [29], which replaces that in the BGK model. The effective relaxation time is computed using the two-equation $k - \epsilon$ renormalization group [30] model. The nonlinearity of the Reynolds stresses can be thus taken into account by this procedure, which is subsequently referred to as very-large eddy simulation (VLES) [31].

The lattice-Boltzmann scheme is applied on a unit lattice defined as *voxel*. The dimension of this volumetric element in adjacent resolution regions of the simulation domain varies by a factor of 2. Surface elements referred to as *surfels* are used to discretize surfaces of solid bodies in the positions where they are intersected by a voxel. The fluid particle interaction with the solid surface is governed by the wall-boundary condition, such as particle bounce-back process for no-slip wall and specular reflection for slip wall [32]. The wall-shear stress is approximated by means of a wall function applied on the first wall-adjacent grid. The function is based on the generalized law-of-the-wall model [33], extended to consider the effects of pressure gradient and surface roughness.

The Ffowcs-Williams and Hawkings (FW-H) acoustic analogy [34] in the formulation 1A of Farassat and Succi [35] with forward-time solution [36] has been utilized to compute the far-field noise. The sound sources have been considered both on a permeable surface enclosing the coated cylinder in the near-field region, with the exception of the side intersecting the body wake. In the former application, the contribution of dipole sources at the surface of solid objects and of quadrupole sources in the turbulent-flow field have been considered, whereas, in the latter, only the dipole sources acting on the cylinder have been taken into account.

2. Set-up and post-processing

A sketch with a side view of the simulation domain is shown in Fig. 3. The domain is a parallelepiped with dimensions of $42.75\,d \times 31.50\,d \times 0.50\,d$. The origin of the reference system is at the cylinder center, with axes x in the streamwise direction, y in the vertical direction, and z in the spanwise direction. The free-stream velocity of $U_0 = 30\,\mathrm{m\,s^{-1}}$ is obtained by prescribing the mass flow at the inlet. A zero-velocity inlet condition is imposed on the domain boundaries with the exception of the downstream face, where the outlet is assigned with a static pressure of 100 kPa. In addition, all the solid surfaces are defined as no-slip walls. An acoustic buffer region is introduced, starting $32\,d$ away from the cylinder to prevent the sound waves from being reflected by the boundaries. Periodic boundary conditions have been imposed on the sides of the domain, while velocity boundary condition is used at the inlet and pressure boundary conditions at the outlet.

A total of 13 voxel refinement regions are defined in the simulation domain, with the finest grid dimension being 8×10^{-3} mm for the small cylinders in the coating. This implies that 30 voxels are assigned along the bare-cylinder diameter, and the resulting average y^+ is 25 on the body surface. Overall, the simulation domain is discretized in 200×10^6 voxels in the finer configuration.

Both permeable and solid formulations of the FW-H analogy are used to compute the far-field noise. The solid formulation also includes the surfaces of the cylinders constituting the flow-permeable cover. The acoustic pressure is acquired on the permeable FW-H surface with a sampling frequency of 29.5 Hz, while the surface pressure and quantities in the flow field have been recorded at a rate of 15 kHz. Welch's method with blocks of 2^9 samples windowed through a Hanning weighting function having a 75 % data overlap has been used to obtain the power spectral densities with a frequency resolution of approximately 30 Hz. A physical time step of 3.31×10^{-8} s for 100 flow passes along the cylinder has been used to carry out the simulation, resulting in a total physical time of 0.3 s. Data are saved after an initial transient of 0.1 s. The simulation time is also equal to 30 vortex-shedding cycles. Finally, the validation and grid-convergence analysis of the generated numerical dataset is reported in Appendix V.

D. Numerical beamforming algorithm

1. Microphone array & conventional beamforming

In this study, we use Conventional Beamforming (CB) (also referred to as cross-spectral beamforming). Fluctuating pressures in the acoustic far-field are calculated using FW-H at 100 equispaced points along a line spanning $x = -8d$ to $12d$ along $y = 8d$. The array used for beamforming is presented in Fig. 4. A Point Spread Function (PSF) is an array performance metric [37] that involves testing a unit strength monopole source at the center of the scanning grid. First, a grid of potential sources (also known as a scanning grid) must be established. This is computed over a grid (often referred to as a scanning grid) that is composed of N distinct points. The grid is typically square, i.e., $\sqrt{N} \times \sqrt{N}$. However, in this study, acoustic propagation is restricted to two dimensions, and thus, a scanning line of N-points, i.e., an $N \times 1$ vector, is used. This scanning line extends between $x/d = -2$ to 1 and $y/d = 0$ using $N = 200$-points, giving a

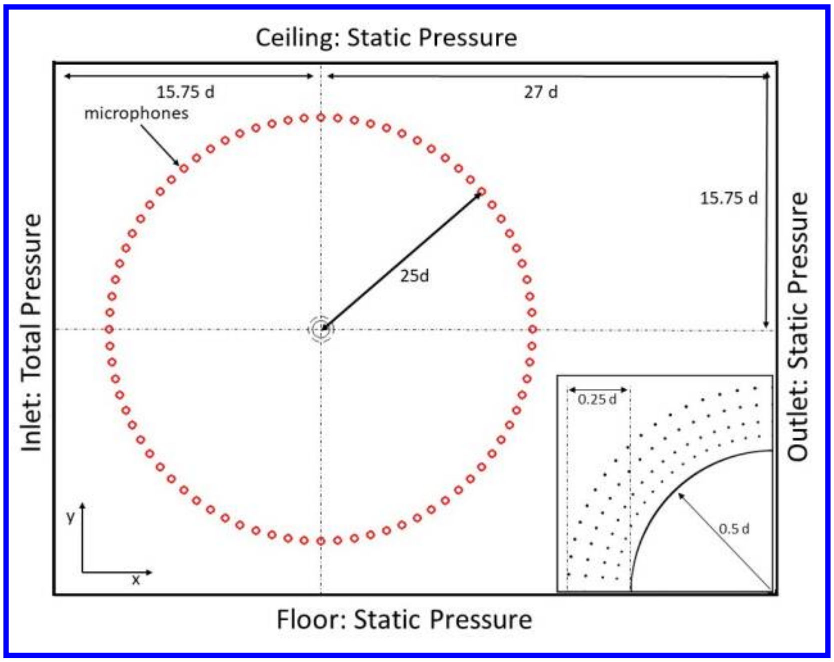

Fig. 3 Numerical setup designed to investigate the coated-cylinder flow-induced noise. An enlargement of the structured cover architecture is visible in the bottom-right corner. The microphone array used to compute the acoustic data is depicted in red.

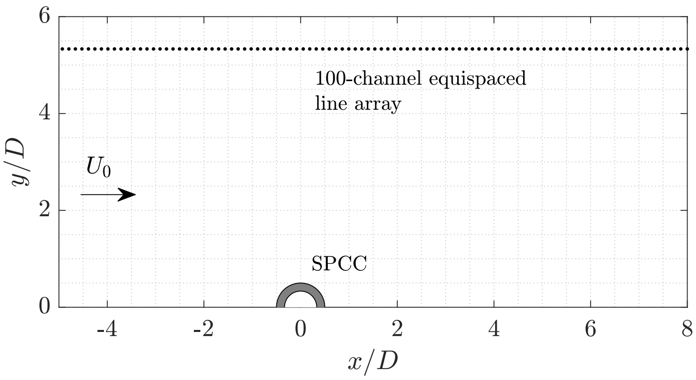

Fig. 4 100-channel equispaced line array used for acoustic beamforming, placed at $x = -8d$ to $12d$ and $y = 8d$, where d is the diameter of the inner cylinder.

resolution of 0.6 mm, corresponding to $x/D = 0.01$. Second, a spherical wave source, i.e., a monopole, of unit source strength in still conditions is simulated. The propagation of this wave to the array plane can be represented as $\mathbf{p}$, a vector of complex pressures (Pa^2) in the frequency domain ($M \times 1$ vector), defined as

$$\mathbf{p} = \frac{1}{4\pi\,|\mathbf{r_s}|}\mathrm{e}^{-\mathrm{j}2\pi f \mathbf{r}_s/c_0}, \tag{7}$$

where f (Hz) represents the source frequency, $c_0 = 343\,\mathrm{m\,s^{-1}}$ and m denotes the microphone number ranging from 1 to M, where M is the number of microphones in the array. The vector $\mathbf{r}_s$ links the simulated source location to each of the microphone coordinates in the array plane. The complex pressures at each microphone generated in Eq. (7) are used to produce a cross-spectral matrix (CSM) [38], C (Pa^2), which is an $M \times M$ matrix defined as

$$C = \mathbf{p}\mathbf{p}^H, \tag{8}$$

where H represents the complex transpose and conjugate. The diagonal entries are set to zero to remove the autospectra from the matrix. Steering vectors, $\mathbf{v}$, relate the expected propagated pressure from a source to each microphone, m, in the array [37–39]. The steering vector formulation for the m^{th} microphone used here [38] is an $N \times 1$ array defined as

$$\mathbf{v} = \frac{1}{4\pi\,|\mathbf{r_m}|}\mathrm{e}^{-\mathrm{j}2\pi f \mathbf{r}_m/c_0}, \tag{9}$$

where $\mathbf{r}_m$ is the vector between the scanning grid point to the microphone m. The cross-spectral beamforming output, Y (Pa^2), [38] is computed computed over the N-scanning grid points via

$$Y = \frac{\mathbf{v}^H\mathbf{C}\mathbf{v}}{M^2 - M}, \tag{10}$$

where the PSF is $|Y|$ when the simulated monopole source is located at $(x, y) = (0, 0)$.

2. Array pairing

A line array with equispaced sensors will generate a PSF with many strong sidelobes mirrored about the main lobe, which is problematic for the estimation of acoustic source position(s) and amplitudes. To reduce the sidelobe amplitudes, a simple iterative array design approach is used (analogous to image stacking), which follows similar, but more complex, array pairing methodologies [40, 41]. A random permutation of $M = 50$ to 90 microphones is used here within the line array of 100 channels. The PSF of this computation (namely Y_1) is calculated and recorded. Another random permutation of microphones is then used to generate Y_2, and this overall procedure is repeated until Y_{15} is created. Note that the use of 15 iteration stages is arbitrary; yet, as shown in the results of the PSF and aeroacoustic

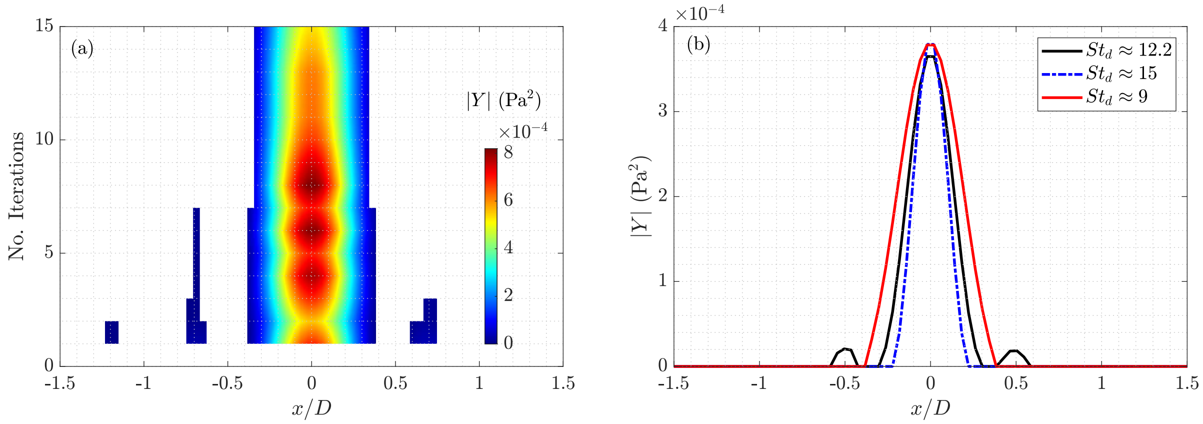

Fig. 5 PSF of a simulated monopole source at $(x, y) = (0, 0)$. (a) Evolution of the PSF with increasing iterations at St_d ≈9 and (b) PSFs recorded after 15 iterations at three distinct frequencies, corresponding to St_d ≈9, 12.2. and 15. Note that these Strouhal numbers correspond to the lower, peak, and upper limits of the HF-Band from the numerical simulation, respectively (see Fig. 10).

source localization in Fig. 5, it is typically adequate to remove most sidelobes and prevent any degradation of the main lobe. By pairing arrays that have sidelobes in different places, yet main lobe peak values at the same position, the paired output is significantly cleaner than an unpaired output. The final PSF, Y, is then computed as

$$Y = \{Y_1 \odot Y_2 \odot \ldots \odot Y_{15}\}^{\odot \frac{1}{15}}, \tag{11}$$

where the $\odot$ terms are element-wise multiplication (Hadamard product), and the $1/15^{\text{th}}$ root of the total product recovers the true source strength. The iterative stages using this method are illustrated in Fig. 5(a), revealing how the PSF evolves with increasing iterations. Sidelobes are present during the first 8 iterations, and the main lobe width is seen to narrow with increasing iterations. Figure 5(b) reveals the PSF of three different frequencies, revealing the array performance consistency. Only some weak grating lobes exist at $St_d \approx 12.2$; in all cases, the main lobe is symmetric about $x/D = 0$, and the peak amplitude of each PSF is nearly constant. Note that the methodology for generating a PSF and using the far-field data from the numerical simulation of the SPCC is identical; the only change is that the pressure vector matrix in Eq. (7) is replaced with the recorded pressures from the numerical simulation.

III. Results

A. Potential-flow analysis

The velocity field that the small-scale cylinders are subject to can be estimated using the potential flow theory of flow around a wholly porous cylinder, presented by Power et al. [22]. A similar approach was used by Zamponi et al. [42] to model the distortion experienced by turbulence in the interaction with a porous leading edge. In polar coordinates, the velocity field is

$$\begin{aligned} \frac{u_r}{U_0} &= \left(1 - \frac{1}{r^2}\right)\cos\theta - 2K^*\frac{1}{r^3}\cos(2\theta); \\ \frac{u_\theta}{U_0} &= -\left(1 + \frac{1}{r^2}\right)\sin\theta - 2K^*\frac{1}{r^3}\sin(2\theta), \end{aligned} \tag{12}$$

where

$$K^* = \frac{2k_0 U_0}{\nu D} \tag{13}$$

is a dimensionless permeability parameter, where k_0 is the permeability of the porous medium and ν is the kinematic viscosity. The use of this potential flow methodology is only valid if the K^*-value is low [42]. As k_0 of the published SPCC is unknown, we use the comparison between the approach velocity to the cylinder on the windward surface with published experimental SPCC data to estimate it. By using a value of $K^* \approx 0.12$, excellent agreement between SPCC experimental results (up to $x/D = -0.5$) of $\overline{u}/U_0$ is recorded, as shown in Fig. 6(a). For reference, the larger potential flow field using Eq. (12) is provided in Fig. 6(b).

As the agreement between the TPIV data and potential flow model is observed for $x/D \leq 0.5$, we will restrict the use of the potential flow model to the outer diameter only and anticipate that the potential flow equations will overestimate the local velocity and thus the vortex shedding frequencies and acoustic intensity. By restricting $r = 1$ in Eq. (12) such that the only variable is θ, we arrive at

$$\frac{u_r}{U_0}|_{r=1} = -2K^*\cos(2\theta), \quad \frac{u_\theta}{U_0}|_{r=1} = -2\sin\theta - 2K^*\sin(2\theta), \tag{14}$$

and, therefore, the velocity amplitude is

$$|u(\theta)| = 2U_0\sqrt{K^{*^2} + \sin^2\theta + 2K^*\sin\theta\sin 2\theta}, \tag{15}$$

which can then be substituted into Eq. (2) used to quantify $\boldsymbol{\Omega}(\theta)$ as

$$\Omega(\theta) = \frac{2StU_0}{d}\sqrt{K^{*^2} + \sin^2\theta\,(1 + 4K^*\cos\theta)}. \tag{16}$$

From Eq. (16), the frequency range of the HF-Band can be estimated. It can be seen that the small-scale cylinder at $\theta = 0$ will shed the lowest frequency vortices at $\Omega(0) = 2\,StU_0K^*/d$ Hz. The highest frequency vortices will be shed at

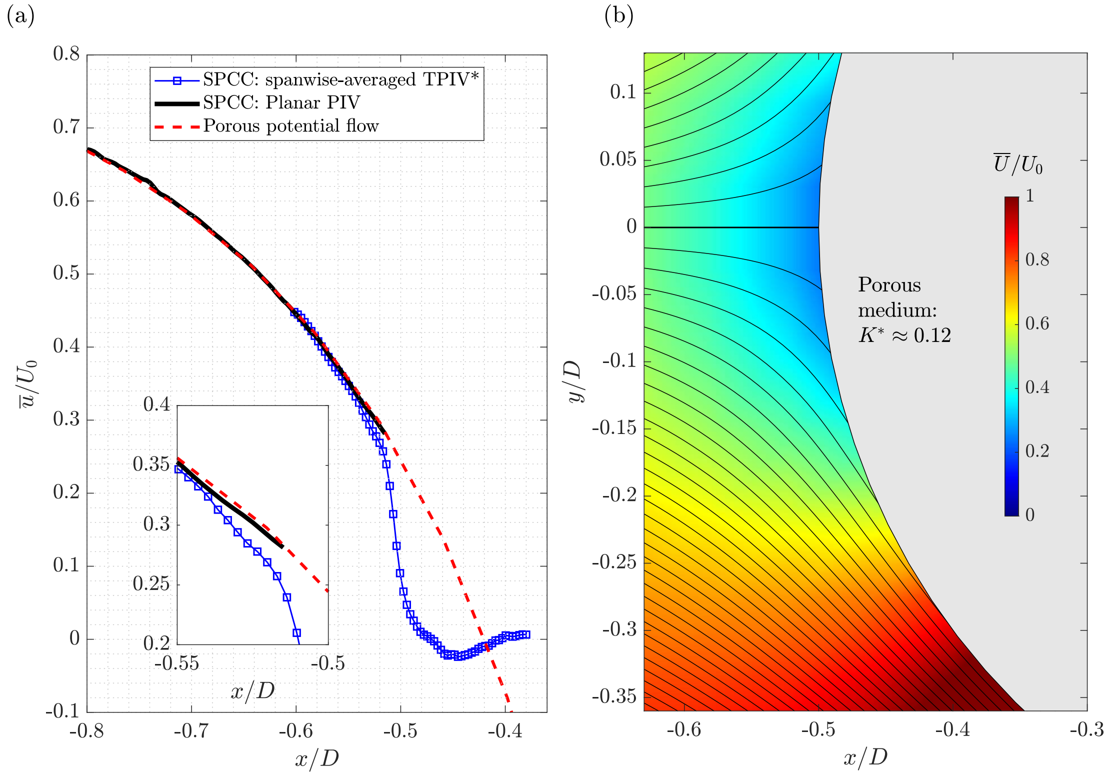

Fig. 6 (a) Comparison of $\overline{u}/U_0$ along $y/D \approx -0.2$ between SPCC planar PIV data and TPIV data (from Arcondoulis et al. [10]) and potential flow solutions of a fully-porous cylinder via the methodology of Power et al. [22] (assuming $K^* = 0.12$). (b) Potential flow solution of $K^* = 0.12$.

the point of maximum velocity; yet, it is not immediately where the maximum total velocity occurs due to the presence of the $\cos(\theta)$ term in Eq. (16) (from the $\sin(2\theta)$ term in Eq. (15)) induced by permeability. Using $\varphi(\theta) = d$ in Eq. (3), the acoustic intensity, $I(\theta)$, due to each small-cylinder at position θ with frequency $\Omega(\theta)$ is calculated as

$$I(\theta) \sim \frac{64\rho_0 U_0^6 d^2}{c_0^3}\left(K^{*^2} + \sin^2\theta\,(1 + 4K^*\cos\theta)\right)^3, \tag{17}$$

and Fig. 7(a) presents the values of $\Omega(\theta)$ (Hz) and acoustic intensity, $I(\theta)$ (W/m^2), respectively, using the parameters outlined in Section C. Both curves possess a maximum at $\theta \approx 75°$, revealing that the cylinder permeability shifts the peak velocity amplitude at the outer diameter from 90° to 75°. The values of $\Omega(\theta)$ are likely to significantly overestimate the vortex shedding frequencies. This is because incompressible potential flow models break down in separated flow regions [43] and typically overestimate the streamwise flow acceleration and near-wall flow fields in areas where boundary layer separation is anticipated (for example: the flow around a cylinder modeled by potential flow has a peak velocity of $2U_0$ at $r = 1$ and $\theta = 90°$ whereas in reality for a cylinder with $Re \geq 1000$ the flow near the surface at $\theta = 90°$ is dominated by boundary layer development.)

To determine the values of θ at which the peak vortex-shedding frequency and associated peak acoustic intensity occur, solutions to $dI/d\theta = 0$ were sought for varying values of θ and K^* and are plotted in Fig. 7(b). If $K^* = 0$, i.e., the cylinder is solid, then the maximum shedding frequency and acoustic intensity occurs at $\theta = 90°$, where $U = 2U_0$. With increasing K^*, the point of maximum frequency and intensity moves further windward, and the local velocity decreases from the solid case. With further increasing (and unrealistic) values of K^*, θ approaches approximately 55°. It is assumed that this critical angle converges to a value distant from 0° due to the influence of the stagnation region of the cylinder as a whole.

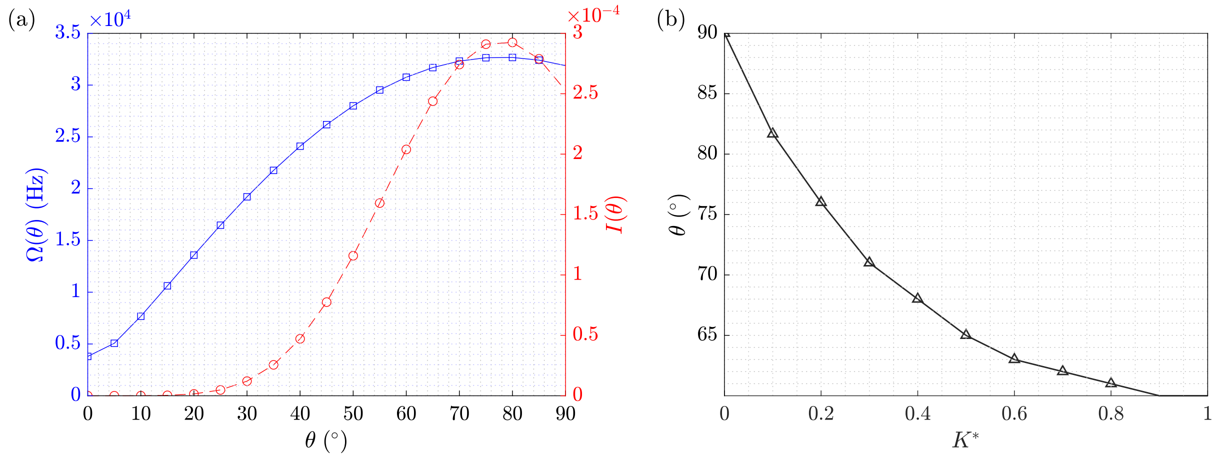

Fig. 7 (a) Frequency response, $\Omega(\theta)$ (Hz) and acoustic intensity, $I(\theta)$ ($\mathrm{W/m^2}$), of the 2-D SPCC using the potential flow velocity field and only considering the outer porous layer with cylinder diameters d_4. (b) Solutions to $dI/d\theta = 0$ for varying K^* values to reveal the circumferential position of maximum acoustic intensity, $I_{\max}$.

Due to the presence of a 6th power of velocity term and the relatively low values of K^*, it may be convenient to express the acoustic intensity using a second-order approximation in K^*, given by

$$I(\theta) \sim \frac{64\rho_0 U_0^6 d^2}{c_0^3} \sin^6\theta\,(1 + 12K^*\cos\theta) + O({K^*}^2), \tag{18}$$

and via Eq. (6) the total acoustic intensity can calculated via integration with respect to θ, yielding

$$I_T \sim \frac{128\rho_0 U_0^6 d^2}{c_0^3}\left(\frac{15\pi}{96} + \frac{12K^*}{7}\right) + O({K^*}^2). \tag{19}$$

B. Simulation analysis

1. Velocity flow field & turbulent kinetic energy

The time-averaged velocity of the 2-D SPCC, obtained via the LBM simulation, is presented in Fig. 8(a). The freestream velocity travels from left to right and interacts with the small-scale cylinders, where many small cylinders are seen to possess a shear layer on both sides and a small wake region. Dashed lines are drawn through each cylinder in Fig. 8(a). The slope of these lines are selected to align with the incident flow direction onto the individual small-scale cylinder. This is done by estimating the wake width and then finding the line that passes through the point of zero velocity. Flow field data are recorded along these lines via linear interpolation from the 2-D flow field that is computed over an equispaced grid. A smoothing function is then applied to the data along these lines, herein referred to as ζ-lines.

The turbulent kinetic energy (TKE) is plotted in Fig. 8(b), where TKE, k (%) is calculated via

$$k = \frac{1}{2}\left(\frac{\overline{u'u'} + \overline{v'v'}}{U_0^2}\right) \times 100\ (\%), \tag{20}$$

and u' and v' are the fluctuating velocity components of the streamwise and vertical flow fields, respectively. Figure 8(b) reveals that the strongest TKE values, $k \geq 10$ (%), occur within a circumferential range of $45^\circ \leq \theta \leq 75^\circ$, with the maximum TKE value recorded at $\theta \approx 65^\circ$. Interestingly, significant TKE values are observed for all porous layers. This is explained by observing the time-averaged total flow field in Fig. 8(a), where the flow between the porous layer is dominated by the radial flow component, as the porous layers act as flow straighteners. It should be noted that some of the small-scale cylinders are colored gray: these cylinders possess a local Reynolds number of $Re_{d_i} < 300$, which is below the sub-critical flow regime and are no longer considered in the subsequent analysis. The local flow around these cylinders is dominated by the larger stagnation region of the solid inner cylinder.

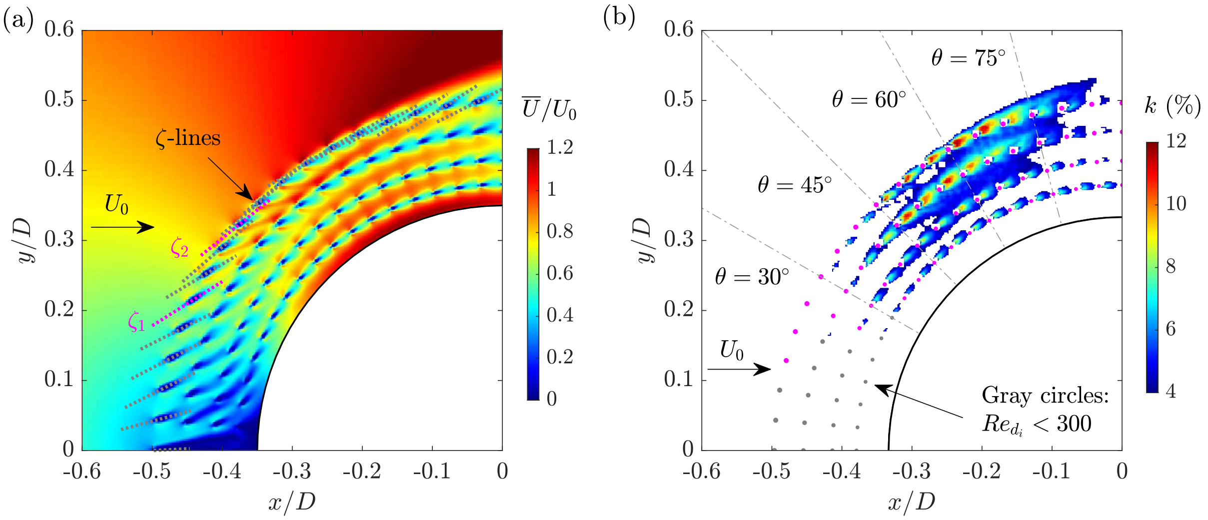

Fig. 8 Flow-field results of the LBM simulation: (a) Normalized time-averaged velocity, $\overline{U}/U_0$, with ζ-lines plotted for the outer layer cylinders and (b) $k \geq 4$ (%), where the centers of the small-scale cylinders are denoted by magenta dots. Gray dots denote small-scale cylinders that are subject to flow fields below the sub-critical flow regime ($Re_{d_i} < 300$).

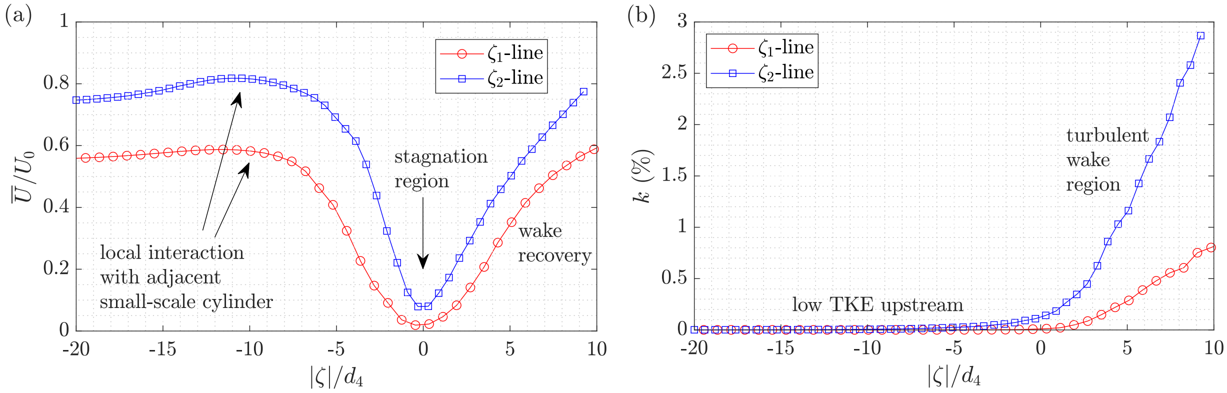

Fig. 9 (a) $\overline{U}/U_0$ and (b) k (%), plotted along two ζ-lines, ζ_1 and ζ_2, identified in Fig. 8. The x-axes are normalized by the small-scale cylinder diameter, d_4. Flow is in the positive x-direction.

In Fig. 8(a), two of the ζ-lines are labelled as ζ_1 and ζ_2. The normalized velocity, $\overline{U}/U_0$, plotted along them is presented in Fig. 9(a). For both ζ-lines, the velocity deceleration toward the windward side of the cylinder is clear, the stagnation region is observed, and the wake recovery is also shown. The TKE values along the ζ-lines in Fig. 9(b) reveal that there is negligible TKE upstream of each small-scale cylinder. In addition, the TKE grows in a near-linear manner with increasing downstream distance from the leeward side of the cylinder. These data clearly reveal that the flow around these two small-scale cylinders possesses similar time-averaged velocity properties as a solitary cylinder placed in the freestream, which supports the hypothesis that the individual small-scale cylinders (at least at the outer diameter) will shed vortices and generate tonal noise

2. Small-cylinder array acoustic response

The far-field acoustic spectra recorded by a microphone placed at $(x, y) = (0, 8d)$ is presented in Fig. 10. The comparison of this result with the experimentally obtained HF-Band spectra illustrated in Fig. 1 shows similar spectral characteristics and frequency range of the band. The peak value is observed at $St_d \approx 12.2$, which is within 10% of other SPCC studies [16, 18, 25]. The amplitude range of the HF-Band in Fig. 10 is approximately 76 dB − 58 dB = 18 dB,

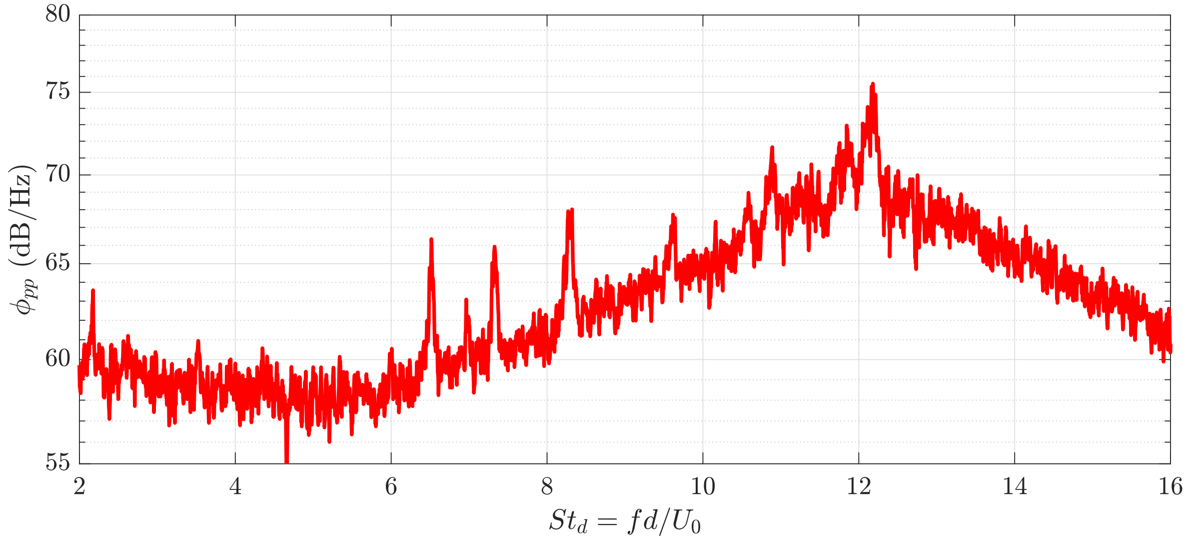

Fig. 10 Far-field fluctuating acoustic pressure spectrum, ϕ_{pp} (dB Hz^{-1}), of the SPCC, recorded by a microphone placed at $(x, y) = (0, 8\,d)$. The frequency axis is normalized by the Strouhal number of the inner cylinder diameter, d. The reference pressure is 20 µPa.

which shows very good agreement with the amplitude range of the SPCC spectra in Fig. 1 being approximately 15 dB and 17 dB for $U_0 = 20\,\mathrm{m\,s^{-1}}$ and $50\,\mathrm{m\,s^{-1}}$, respectively. This very good agreement provides confidence in the simulated results and strengthens the validity of this analysis in terms of explaining the experimentally obtained results.

The velocity immediately upstream of each small scale cylinder along its respective ζ-line is used to calculate the vortex shedding frequency and therefore Strouhal number (St_d) of each small-scale cylinder. These values are presented in Fig. 11(a). At $\theta = 0°$, many of the cylinders are below the sub-critical flow regime and therefore do not contribute to the vortex shedding spectra. With increasing θ-values, the shedding frequency increases for all porous layers (except Layer 3), up to a critical angle of 60° where the maximum vortex shedding frequency per layer is observed. Layer 3 represents a flow transition within the porous region, where Layer 4 is subject to a significant radial flow component (similar to a large, solid cylinder), which has been converted mainly into a radial component due to flow straightening at Layers 1 and 2.

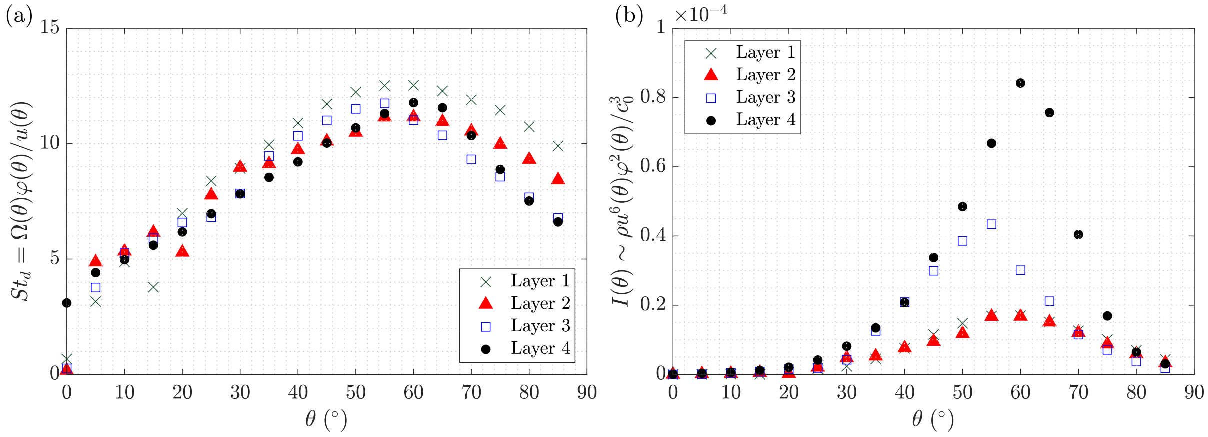

Fig. 11 Calculations using the LBM-calculated flow field for each small-scale cylinder: (a) Strouhal number, $St_d(\theta)$, via Eq. (2) and (b) Acoustic intensity, $I(\theta)$, via Eq. (3.)

As the boundary layer height around the cylinder grows with increasing θ-values, the local flow field around each small cylinder decreases, which explains the reduction in vortex-shedding frequency for $\theta > 60°$, and the rate of decrease in shedding frequency with respect to θ is greatest for the outer-most porous layer. Layer 1 (the innermost layer) yields the highest Strouhal number due to the combination of Layer 1 having the smallest diameter cylinders and flow straightening between Layer 1 and the solid inner diameter (refer to Fig. 8). The acoustic intensity values of corresponding vortex-shedding frequencies are presented in Fig. 11(b), where it is clear that Layer 4 generates the highest vortex-shedding noise at the critical angle of $\theta = 60°$, and Layer 3 generates a notable contribution at $\theta = 55°$. Layers 1 and 2 appear not to contribute significantly to the overall acoustic intensity, mainly due to their lower total incident velocity and smaller diameters. Nonetheless, they do not exhibit a distinct peak like Layers 3 and 4, but their maxima also occur at $\theta = 60°$. From the presented data, it is anticipated that the region of greatest acoustic intensity of the studied SPCC should lie within $\theta = 45°$ and $70°$, which is consistent with the angular region of peak TKE shown in Fig. 8(b).

The propagation of the acoustic source into far-field pressure is now calculated. The acoustic intensity is converted into acoustic power (dB) (ref. 10^{-12} W) for each small-scale cylinder in the n^{th}-layer via

$$I_{\text{dB}}(\theta) = 10\log_{10}\left(I(\theta)\frac{\pi d_n^2}{10^{-12}}\right), \tag{21}$$

and the acoustic pressure (dB) recorded at a distance R from the outer diameter of the SPCC is calculated via

$$L_p(\theta) = I_{\text{dB}}(\theta) - 10\log_{10}\left(4\pi R^2\right) \tag{22}$$

where $L_p(\theta)$ values are linked with frequency values $\Omega(\theta)$. In order to create spectral data of ϕ_{pp} (dB Hz^{-1}) with respect to frequency (Hz), a histogram approach was used. The total acoustic intensity of each small-scale cylinder and its corresponding frequency was collated per layer. The frequency range was calculated, and each band was 1/10th the total frequency range. These results are presented in Fig. 12(a). Here, it is clearly seen that Layer 4 generates the greatest far-field acoustic pressure, closely followed by Layer 3, especially at $St_d \approx 8$ to 10. All layers possess peak amplitudes at the highest frequency. Note that Layer 1 is characterized by a slightly higher frequency than the other layers. The summed contribution of all four layers is presented as the gray line in Fig. 12(b). In addition, the contribution of all layers is divided into θ-ranges to determine which circumferential region is responsible for the greatest HF-Band contribution. Clearly, the contribution from $\theta = 30°$ to $60°$ provides the greatest contribution to the HF-Band peak at $St_d \approx 12.2$. Lower frequency content is observed closer to $\theta = 0°$, and, toward the region of boundary-layer separation at $\theta = 60°$ to $90°$, a local maximum in the acoustic spectra is observed at $St_d \approx 10$. Further analysis of these acoustic source positions is conducted in the following section using numerical acoustic beamforming.

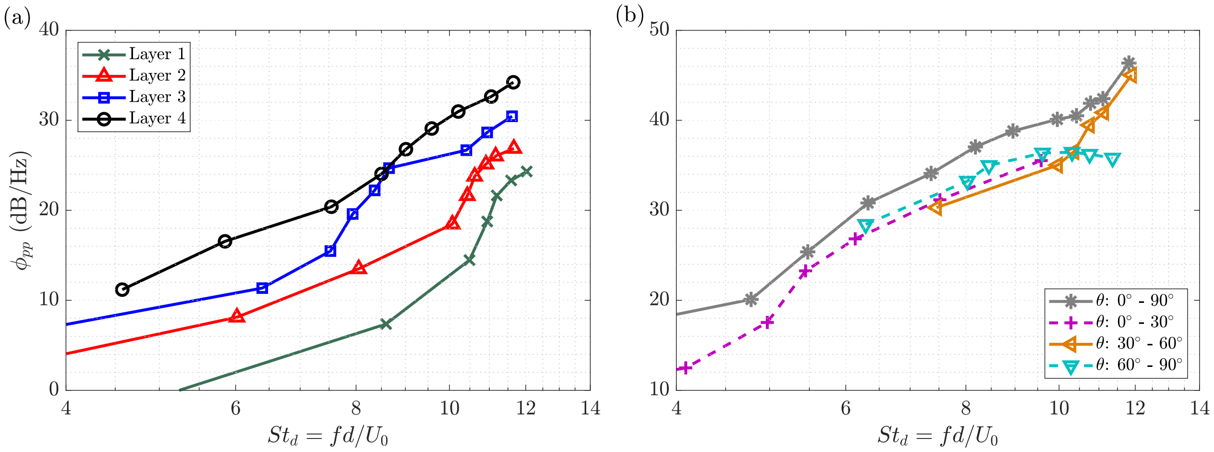

Fig. 12 Summation of acoustic intensity within frequency bands to estimate far-field spectra at 25 d: (a) ϕ_{pp} (dB Hz^{-1}) calculated from the acoustic sources generated from each small-scale cylinder layer and (b) ϕ_{pp} (dB Hz^{-1}) calculated from all layers within specific angular sectors. The reference pressure is 20 µPa.

3. Numerical acoustic beamforming

The numerical acoustic beamforming results are presented in Fig. 13. The maximum acoustic source strength values, $|Y|_{\max}$, were located along the scanning line for frequency range corresponding to $St_d = 9$ to 15. These amplitudes and x/D-positions were recorded and are presented as a scatter plot in Fig. 13(a). To assist the visualization of the relative position of the SPCC, x/D positions and circumferential angles, θ, a schematic diagram of the SPCC is included where the dark shaded ring represents the porous layers and the vertical dashed lines correspond to circumferential positions along the outer diameter, D. The color of the scatter plot corresponds to $|Y|_{\max}$-values. For $9 \le St_d \le 11$, the acoustic sources are centered about $x/D \approx -0.4$. These positions and amplitudes are consistent with the numerical results in Figs. 11 and 12 that showed that the lowest frequency contributions of the HF-Band are generated at $\theta \le 30°$. The peak acoustic strength, $11 \le St_d \le 13$, is typically located within $50° \le \theta \le 75°$, which agrees well with the mathematical results in Fig. 7(a) and the numerical results in Figs. 11 and 12. Higher frequencies within the HF-Band, $13 \le St_d \le 15$,

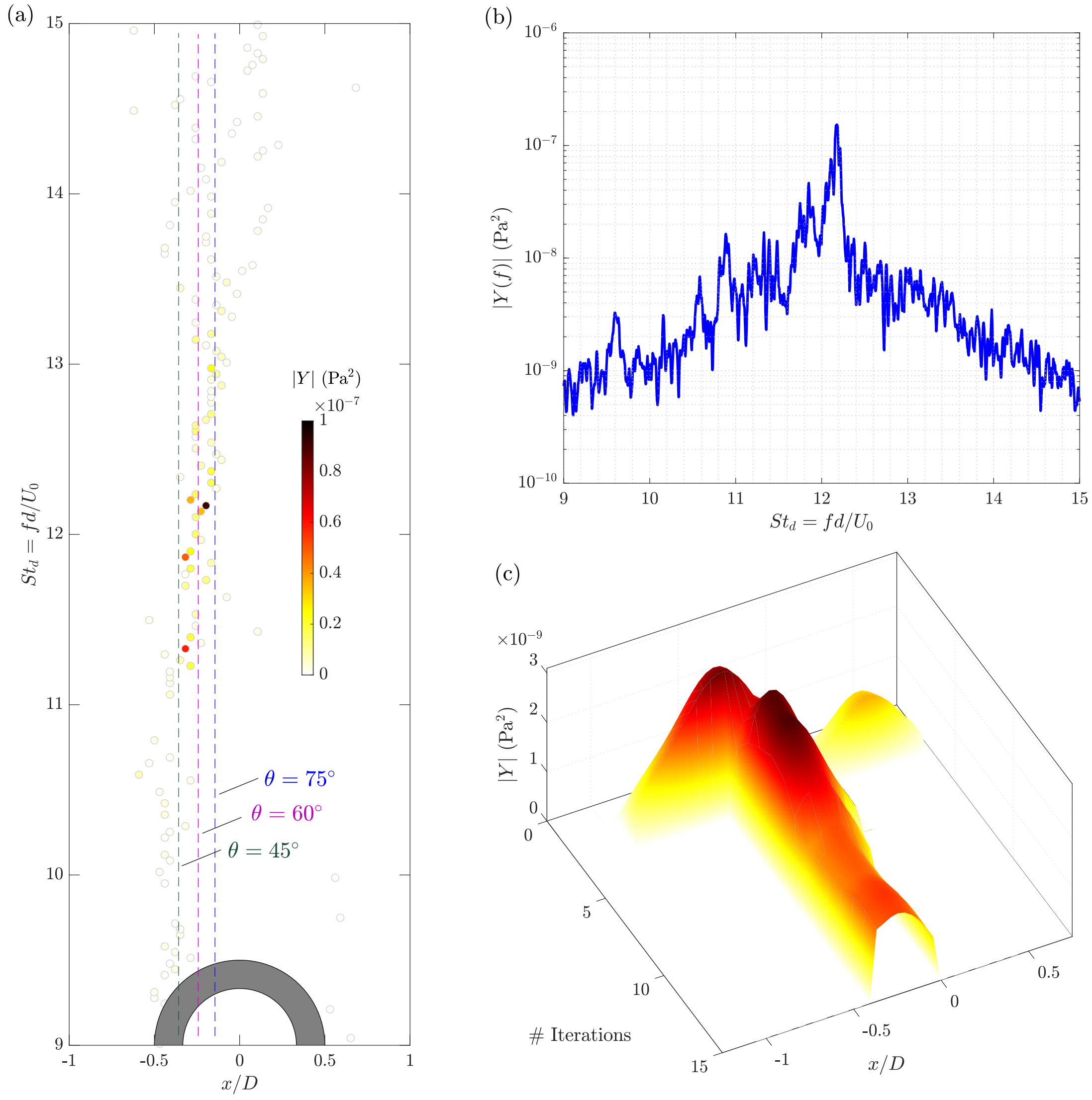

Fig. 13 Acoustic beamforming results: (a) location of maximum acoustic source strength, $|Y|_{\max}$ (Pa^2), in terms of x/D, over a frequency range bounded by $St_d = 9$ to 15. The colorbar represents $|Y|_{\max}$ amplitude, whereas the vertical dashed lines are drawn presenting circumferential positions on the outer SPCC diameter, $\theta = 45°$, 60°, and 75°. Flow is in the positive x-direction. (b) Reconstruction of the acoustic spectra based on $|Y|_{\max}$-values, bounded by $St_d = 9$ to 15. (c) Evolution of $|Y|$ with increasing array pairing iterations for $St_d = 12.2$.

reveal scattered sources near the peak source positions, with some weaker sources located near $x/D = 0$ and some toward the leeward part of the cylinder. It is possible that these sources are generated by a separate, weaker mechanism that may involve the interaction of the turbulent shear layer with the upper surface of the SPCC. Figure 13(b) is a reconstruction of the acoustic spectra using $|Y|_{\max}$-values, which shows excellent agreement with the far-field acoustic spectra shown in Fig. 10. At a single frequency of $St_d = 12.2$, Fig. 13(c) reveals the evolution of the beamformer response with respect to array pairing iterations. It is clearly seen that 15 iterations are sufficient to rid the source map of sidelobes and narrow the main lobe, improving the source resolution.

IV. Extension of the theory to 3-D

An analysis of the high-frequency contributions by a 3-D SPCC, such as the characteristic length scale and adaption of the velocity field to incorporate spanwise flow variation, is briefly outlined here. A representation of an SPCC partial span [12] is presented in Fig. 14(a) that consists of a series of concentric interconnected C-shaped pieces, which creates a self-repeating porous structure in 3-D [12, 16, 25].

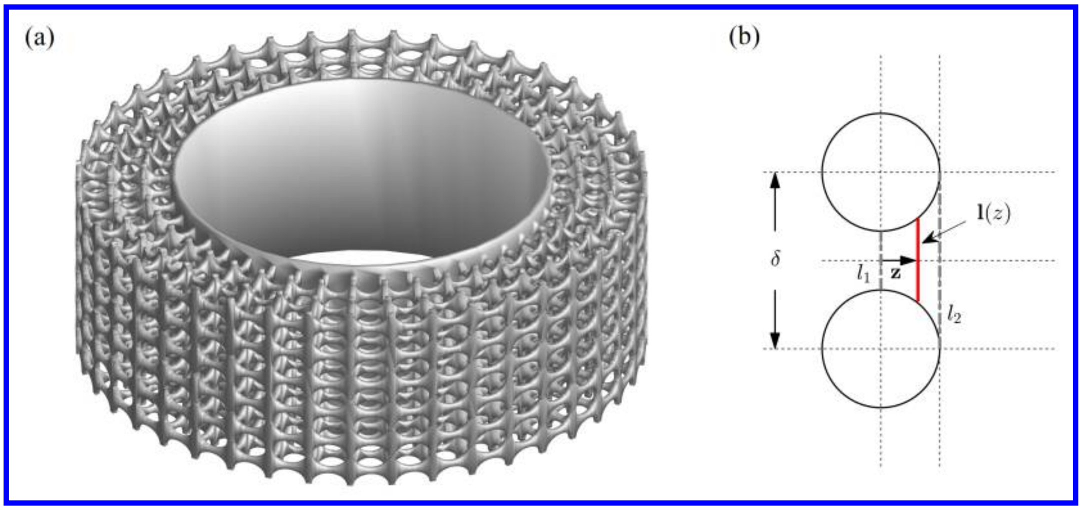

Fig. 14 (a) MATLAB .STL representation of a portion of an SPCC span and (b) schematic diagram of the vortex shedding element and the characteristic length term, $l(z)$.

A. Velocity field

To expand the velocity field into three dimensions, the SPCC spanwise flow component must be included. A TPIV investigation by Arcondoulis et al. [10] presented values of $\overline{u}/U_0$ and $\overline{v}/U_0$ near the SPCC walls that revealed a near-sinusoidal variation in velocity amplitude along a portion of the span. Figure 15 presents the variation of $|\overline{u}|/U_0$ and $|\overline{v}|/U_0$ in the z-direction as the flow approaches the outer windward surface of the SPCC and within the porous layer. The r/h-line follows an open-pore path so that along the z-axis, local minima and maxima corresponding to the flow interacting with a structural member or flowing into the porous layer, respectively, can be observed. Deceleration occurs twice: gradual flow deceleration towards the outer porous layer and rapid deceleration once the flow enters the porous layer, where the narrow region between the grey dashed lines represents the structural member of the pore. The streamwise velocity component is affected by the porous structure: at the structural member, it stagnates, and at the open pores, it flows into the porous layer. Further inside the porous layer, the flow has nearly stagnated at all spanwise locations. The stagnation of the streamwise velocity occurs rapidly between $r/h = 0.82$ and 0.89.

To further pursue the mathematical model in 3-D, only the velocity at the outer diameter is needed, expressed as a function of θ, at a given z-position. The published results of Arcondoulis et al. [10] revealed that the SPCC spanwise flow component is significantly less than the radial and tangential flow fields and has negligible influence on the vortex shedding around the pore structures.

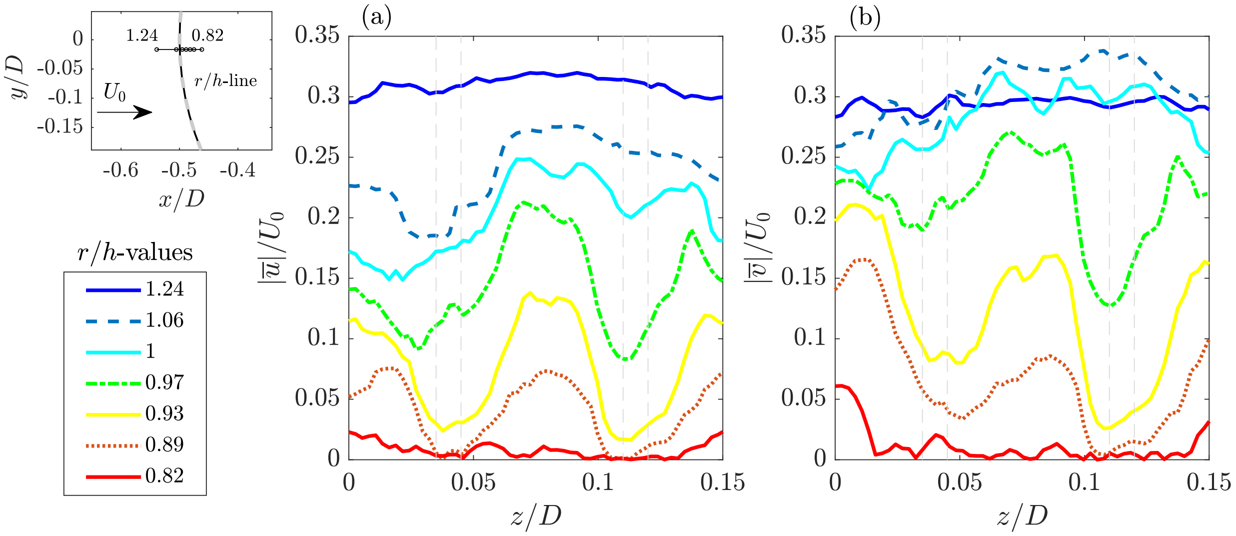

Fig. 15 Variation of the flow field along z/D (spanwise direction), approaching and entering the windward side of the SPCC between $z/D = 0$ to 0.15 (a) $|\overline{u}|/U_0$ and (b) $|\overline{v}|/U_0$. Each line is represented by an r/h-coordinate denoted in the top-left schematic diagram, and the narrow area between the gray dashed lines represents the pore structural members. Image adapted from Arcondoulis et al. [10].

The velocity field is therefore modelled as 2-D, with periodic variation in the z-direction, i.e., each 2-D (xy-plane) flow field can be modified by appending a spanwise term to the velocity function, via

$$
\begin{aligned}
u(r,\theta,z) &= u(r,\theta)\sin\left(\frac{2\pi z}{\delta_z}\right) \\
&= \left[u_r(r,\theta)\sin\left(\frac{2\pi z}{\delta_z}\right), u_\theta(r,\theta)\right] \\
&= \left[u_R(\theta)\alpha(r,\theta)\sin\left(\frac{2\pi z}{\delta_z}\right), u_\theta(r,\theta)\right]
\end{aligned}
\tag{23}
$$

where $u_R(\theta)$ is the radial velocity at the outer diameter, $\alpha(r,\theta)$ is a function to scale the amplitude decay of the internal radial flow field based on radial distance and circumferential angle (as seen in Fig. 15 with decreasing r/h-values) and δ_z is the spacing between pores in the spanwise direction. It is also assumed that the tangential velocity component has negligible spanwise variation [10]. By observation of the time-averaged flow field in Fig. 8(a), the radial component of velocity decreases significantly within the porous layers, and the total flow field is tangential.

B. Characteristic length scale & acoustic intensity

The characteristic length scale function used in Eq. (2) can be broken down into components based on the incident flow field. Firstly, we consider an element of the SPCC geometry, $l(z)$, represented in Fig. 14(b). The relationship between $l(z)$ and the spacing between pores, δ, and the incremental distance in the z-direction can be derived by calculating the distance between the edge of a circle and its tangent offset by a fixed distance. This geometric element is 3-D and has a constant thickness of $t(r)$ (out of the plane of the page). The thickness term is a function of radius, alternating between values of ∞ in the absence of a layer, and t where a layer is present (i.e., in both the simplified and 3-D SPCC cases, there exist four layers and thus four instances where $t(r) = t$ and $t = \infty$ in all other instances). It is assumed that the radial flow component is normal to $l(z)$ and the tangential flow component is normal to $t(r)$. Therefore, $\mathbf{\Omega} = [\Omega_r(r,\theta,z), \Omega_\theta(r,\theta,z)]$ can be expressed as a piece-wise function by splitting the flow field into polar coordinates via

$$
\mathbf{\Omega} = St\left[\frac{|u_R(\theta)|\alpha(r,\theta)}{l(z)}\sin\left(\frac{2\pi z}{\delta_z}\right), \frac{|u_\theta(r,\theta)|}{t(r)}\right]
\tag{24}
$$

The corresponding acoustic intensity can similarly be estimated by considering piece-wise element contributions. Using Eq. (3), we arrive at

$$\mathbf{I} \sim \frac{\rho_0}{c_0^3}\left[u_R^6(\theta)\alpha^6(r,\theta)\sin^6\left(\frac{2\pi z}{\delta_z}\right)l^2(z)\ ,\ u_\theta^6(r,\theta)t^2(r)\right] \tag{25}$$

and, by some algebraic manipulation and substitution into Eq. (4), the total acoustic intensity can be estimated by the summation of the radial and tangential components as

$$I_T \sim \frac{2\rho_0}{c_0^3}\left[\int_{z=0}^{\Delta z} l^2(z)\sin^6\left(\frac{2\pi z}{\delta_z}\right)\int_{\theta=0}^{\frac{\pi}{2}} u_R^6(\theta)\int_{r=\frac{d}{2}}^{R}\alpha^6(r,\theta)\,\mathrm{d}r\,\mathrm{d}\theta\,\mathrm{d}z + \Delta z\int_{r=\frac{d}{2}}^{R} t^2(r)\int_{\theta=0}^{\frac{\pi}{2}} u_\theta^6(r,\theta)\,\mathrm{d}\theta\,\mathrm{d}r\right] \tag{26}$$

where Δz is the SPCC spanwise length. By implementing piece-wise characteristic length scales and in conjunction with 2-D PIV or numerical simulation data, it is plausible that the frequency response and amplitudes of the 3-D SPCC HF-Band, as shown in Fig. 1, could be quantified and derived mathematically. It is future work to test and validate this claim.

V. Conclusions

A hypothesis regarding the high-frequency contributions of an SPCC subject to uniform flow was presented in this paper. A mathematical formulation has been derived to explain the high-frequency noise (often referred to as the HF-Band) based on the assumption that each individual small-scale cylinder comprising the porous layers experiences vortex shedding and generates a vortex-shedding tone linked to the Strouhal number of the small-scale characteristic length. This study used a simplified 2-D SPCC (previously published by Wen et al. [20]) with four layers of small-scale cylinders to mimic the porous properties of other SPCC designs. This model significantly simplifies the derivation of the acoustic frequency response and acoustic intensity, making such an analysis more approachable.

A porous potential flow model was used to estimate the total velocity at the outer diameter of the simplified SPCC. This velocity was used in conjunction with the diameter of the outer layer of small-scale cylinders to estimate their vortex-shedding frequencies and acoustic intensity. By using an approximated permeability value, the peak total velocity amplitude is observed at a circumferential angle of approximately $\theta = 75°$, showing good agreement with published experimental acoustic beamforming results. The HF-Band frequencies, however, were over-predicted due to the limitations of the potential flow model to capture boundary layer development with increasing circumferential angle.

To provide a more accurate estimation of the flow field about the porous layers, a 3-D LBM simulation of the simplified 2-D SPCC was conducted. The simulation revealed that each small-scale cylinder is subject to low turbulent kinetic energy on the windward side and possesses a wake region similar to a single cylinder placed in a freestream flow. This provided some justification for the assumption of individual vortex-shedding processes from each small-scale cylinder. The total velocity imparted onto each small-scale cylinder was quantified and used to develop the acoustic response of the 2-D SPCC. In this case, the cylinder that generated the peak acoustic frequency did not also generate the greatest acoustic intensity: smaller-diameter cylinders in the innermost layer were subject to lower velocities, yet their overall vortex shedding frequency was higher. Nonetheless, both the peak acoustic intensity and frequency were recorded at $\theta = 60°$. By integrating the contributions of each cylinder into frequency bands and by scaling the acoustic intensity into far-field pressure, the acoustic spectra of fluctuating far-field pressure were estimated, showing excellent agreement with the far-field spectra generated using FW-H from the LBM simulation data.

Numerical acoustic beamforming was conducted to further investigate the peak acoustic source location with respect to the circumferential angle. A 100-channel line array was placed in the acoustic far-field and a simplified array pairing method was used to improve the overall PSF of the array. Beamforming results revealed that, for the frequency range of the HF-Band, the peak acoustic source strength was located at $-0.45 \leq x/D \leq 0.25$, with the strongest sources at $St_d \approx 12.2$ located between $\theta = 50°$ to 70°. The combination of the potential flow theory, expansion of the theory to include 2-D LBM flow data, and numerical acoustic beamforming provides a compelling case that the HF-Band is predominately generated by small-scale vortex shedding about the pore structural members on the windward surface of the SPCC (and likely all PCCs) between $\theta = 50°$ to 70°. Such information is invaluable to refine the design of PCCs to ensure that the overall vortex-shedding reduction capability of the PCC is retained while minimising the HF-Band. Future work will include (i) replacing the length scale with a Gaussian distribution to simulate randomized PCCs and (ii) expanding the numerical model into 3-D to determine the spanwise influence of SPCC geometry and incorporate the windward flow field based on published TPIV data, and, via comparison with experimental results, identify the limitations of the model due to interaction noise between the small-scale noise sources.

Appendix: Grid-independence study and validation

The grid-independence study and validation of the developed numerical methodology have been performed by comparing the results of the LBM simulation with the Structure-Resolved-Simulation (SRS) data of Wen et al. [20]. Three computations with different resolutions have been carried out. Refinement factors of 1.875 and 3.75 have been used to increase the resolution with respect to the *coarse* case for the *medium* and the *fine* ones, respectively. The convergence of the numerical simulations has been assessed in terms of velocity profiles at different locations in the wake region and aerodynamic forces, i.e., the lift coefficient C_l and the drag coefficient C_d, computed on the body surface.

Figure 16 illustrates the time-averaged streamwise-velocity profiles u_x extracted at several positions in the cylinder-wake region for the simulations with different levels of refinement. In the immediate vicinity of the body (Fig. 16a), all the LBM results show a satisfactory agreement with the reference SRS data. In particular, the medium and fine computations exhibit no significant difference, suggesting that grid independence has been reached. Nevertheless, this trend is not maintained moving away from the surface. At more downstream x/d locations (Figs. 16b, 16c, 16d), the medium and fine simulations start increasingly diverging. Interestingly, the former show a better agreement with the reference. Moreover, the end of the recirculation region, which corresponds to the outbreak location of the shedding instability [11], appears to be displaced slightly more downstream for the finer simulation than the medium one. This result is confirmed by the horizontal streamwise-velocity profile in Fig. 16e, which demonstrates that the flow region in which u_x is negative, i.e., associated with the flow recirculation, is situated at higher x/d values.

The comparison of the aerodynamic forces exerted on the coated-cylinder surface between the reference SRS data and the present LBM simulations with the finest resolution is reported in Fig. 17, which depicts the power spectral densities of the lift and drag coefficients. The results are presented in function of the Strouhal number based on d and U_∞. While a general satisfactory agreement between the two datasets is obtained for the C_d for $St > 0.3$, the LBM simulations under-predict the reference C_l trend, probably due to the potential lack of convergence mentioned above. A discrepancy is also found in the root-mean-square of the lift coefficient $C_{l,rms}$ and the time-averaged drag coefficient $\overline{C_D}$. The present numerical methodology over-predicts the SRS values in both cases, although the difference may be attributable to the broader frequency range considered in the computation of the statistics. Furthermore, a peak in the power spectral density for the lift is visible at approximately $St = 1.5$ and is associated with the vortex-shedding instability [20].

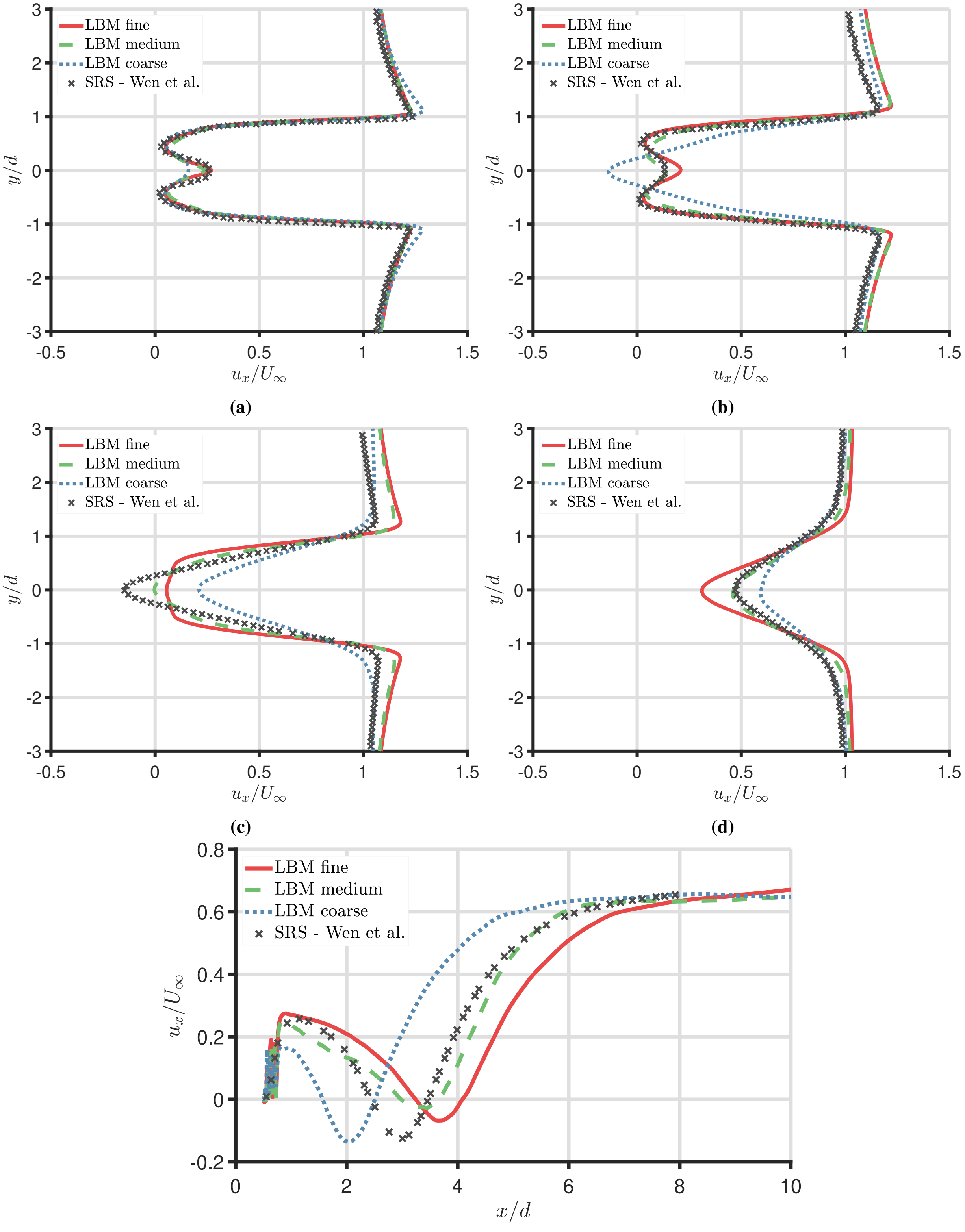

(a) (b)

(c) (d)

(e)

Fig. 16 Comparison of the time-averaged streamwise-velocity profiles at different locations in the wake region of the coated cylinder: (a) $x/d = 1$**; (b)** $x/d = 2$**; (c)** $x/d = 3$**; (d)** $x/d = 5$**; (e)** $y/d = 0$**. SRS data from Wen et al. [20].**

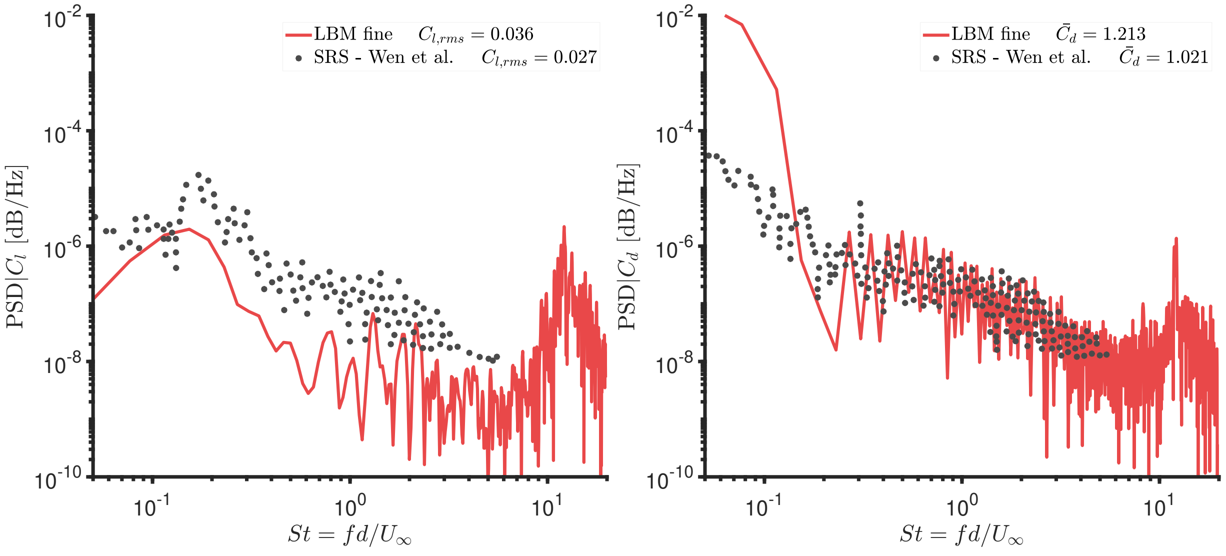

(a) **(b)**

Fig. 17 Comparison of the power spectral densities of the (a) lift and (b) drag coefficients for the coated cylinder. The values of the root-mean-square of the lift coefficient $C_{l,rms}$ and the time-averaged drag coefficient $\bar{C_d}$ for the different configurations are indicated in the legend. SRS data from Wen et al. [20].

References

[1] Etkin, B., Korbacher, G., and Keefe, R. T., "Acoustic radiation from a stationary cylinder in a fluid stream (Aeolian tones)," *The Journal of the Acoustical Society of America*, Vol. 29, No. 1, 1957, pp. 30–36.

[2] Keefe, R. T., "Investigation of the fluctuating forces acting on a stationary circular cylinder in a subsonic stream and of the associated sound field," *The Journal of the Acoustical Society of America*, Vol. 34, No. 11, 1962, pp. 1711–1714.

[3] Vickery, B., and Watkins, R., "Flow-induced vibrations of cylindrical structures," *Hydraulics and fluid mechanics*, Elsevier, 1964, pp. 213–241.

[4] Boorsma, K., Zhang, X., Molin, N., and Chow, L. C., "Bluff Body Noise Control Using Perforated Fairings," *AIAA Journal*, Vol. 47, No. 1, 2009, pp. 33–43.

[5] Geyer, T. F., "Experimental Investigation of Flow and Noise Control by Porous Coated Tandem Cylinder Configurations," *AIAA Journal*, 2022, pp. 1–12.

[6] Sueki, T., Ikeda, M., and Takaishi, T., "Aerodynamic noise reduction using porous materials and their application to high-speed pantographs," *Quarterly Report of RTRI*, Vol. 50, No. 1, 2009, pp. 26–31.

[7] Willmarth, W. W., and Wei, T., "Static Pressure Distribution on Long Cylinders as a Function of the Yaw Angle and Reynolds Number," *Fluids*, Vol. 6, No. 5, 2021, p. 169.

[8] Zdravkovich, M., "Review and classification of various aerodynamic and hydrodynamic means for suppressing vortex shedding," *Journal of Wind Engineering and Industrial Aerodynamics*, Vol. 7, No. 2, 1981, pp. 145–189.

[9] Ran, Y., Deng, Z., Yu, H., Chen, W., and Gao, D., "Review of passive control of flow past a circular cylinder," *Journal of Visualization*, 2022, pp. 1–44.

[10] Arcondoulis, E., Liu, Y., Ragni, D., Avallone, F., Rubio-Carpio, A., Sedaghatizadeh, N., Yang, Y., and Li, Z., "Internal shear layer and vortex shedding development of a structured porous coated cylinder using tomographic particle image velocimetry," *Journal of Fluid Mechanics*, Vol. 967, 2023, p. A17.

[11] Zamponi, R., Avallone, F., Ragni, D., Schram, C., and Van Der Zwaag, S., "Relevance of quadrupolar sound diffraction on flow-induced noise from porous-coated cylinders," *Journal of Sound and Vibration*, Vol. 583, 2024, p. 118430.

[12] Arcondoulis, E. J. G., Liu, Y., Li, Z., Yang, Y., and Wang, Y., "Structured porous material design for passive flow and noise control of cylinders in uniform flow," *Materials*, Vol. 12, No. 18, 2019, p. 2905.

[13] Arcondoulis, E., and Liu, Y., "The effect of porosity on the porous coated cylinder diameter," *Proceedings of ACOUSTICS*, Vol. 7, 2018.

[14] Xia, C., Wei, Z., Yuan, H., Li, Q., and Yang, Z., "POD analysis of the wake behind a circular cylinder coated with porous media," *Journal of Visualization*, Vol. 21, No. 6, 2018, pp. 965–985.

[15] Geyer, T. F., "Experimental evaluation of cylinder vortex shedding noise reduction using porous material," *Experiments in Fluids*, Vol. 61, No. 7, 2020, pp. 1–21.

[16] Arcondoulis, E. J. G., Geyer, T. F., and Liu, Y., "An investigation of wake flows produced by asymmetrically structured porous coated cylinders," *Physics of Fluids*, Vol. 33, No. 3, 2021, p. 037124.

[17] Scholz, M. M., Arcondoulis, E., Woodhead, P. C., Chong, T. P., and Smith, E., "Structured porous coated cylinder modifications based on internal flow field data," *AIAA AVIATION 2023 Forum*, 2023, p. 3926.

[18] Maryami, R., Arcondoulis, E. J., Liu, Q., and Liu, Y., "Experimental near-field analysis for flow induced noise of a structured porous-coated cylinder," *Journal of Sound and Vibration*, Vol. 551, 2023, p. 117611.

[19] Norberg, C., "Fluctuating lift on a circular cylinder: review and new measurements," *Journal of Fluids and Structures*, Vol. 17, No. 1, 2003, pp. 57–96.

[20] Wen, K., Arcondoulis, E. J., Li, Z., and Liu, Y., "Structure resolved simulations of flow around porous coated cylinders based on a simplified pore-scale model," *Aerospace Science and Technology*, Vol. 119, 2021, p. 107181.

[21] Curle, N., "The influence of solid boundaries upon aerodynamic sound," *Proceedings of the Royal Society of London. Series A. Mathematical and Physical Sciences*, Vol. 231, No. 1187, 1955, pp. 505–514.

[22] Power, H., Miranda, G., and Villamizar, V., "Integral-equation solution of potential flow past a porous body of arbitrary shape," *Journal of Fluid Mechanics*, Vol. 149, 1984, pp. 59–69.

[23] Zamponi, R., Avallone, F., Ragni, D., and van der Zwaag, S., "On the Aerodynamic-Noise Sources in a Circular Cylinder Coated with Porous Materials," *28th AIAA/CEAS Aeroacoustics 2022 Conference*, 2022, p. 3042.

[24] Zamponi, R., Ragni, D., Van Der Zwaag, S., and Avallone, F., "Innovative coatings for reducing flow-induced cylinder noise by altering the sound diffraction," *Physics of Fluids*, Vol. 35, No. 12, 2023, p. 127120.

[25] Arcondoulis, E. J. G., Geyer, T. F., and Liu, Y., "An acoustic investigation of non-uniformly structured porous coated cylinders in uniform flow," *The Journal of the Acoustical Society of America*, Vol. 150, No. 2, 2021, pp. 1231–1242.

[26] Sharma, S., Geyer, T. F., and Arcondoulis, E. J., "On the influence of porous coating thickness and permeability on passive flow and noise control of cylinders," *Journal of Sound and Vibration*, 2023, p. 117563.

[27] Chen, H., Chen, S., and Matthaeus, W. H., "Recovery of the Navier-Stokes Equations Using a Lattice-Gas Boltzmann Method," *Phys. Rev. A*, Vol. 45, No. 8, 1992, pp. R5339–R5342.

[28] Bhatnagar, P. L., Gross, E. P., and Krook, M., "A Model for Collision Processes in Gases. I. Small Amplitude Processes in Charged and Neutral One-Component Systems," *Physical Review*, Vol. 94, No. 3, 1954, pp. 511–525.

[29] Chen, H., Kandasamy, S., Orszag, S., Shock, R., Succi, S., and Yakhot, V., "Extended Boltzmann Kinetic Equation for Turbulent Flows," *Science*, Vol. 301, No. 5633, 2003, pp. 633–636.

[30] Yakhot, V., and Orszag, S. A., "Renormalization Group Analysis of Turbulence. I. Basic Theory," *Journal of Scientific Computing*, Vol. 1, No. 1, 1986, pp. 3–51.

[31] Chen, H., Orszag, S. A., Staroselsky, I., and Succi, S., "Expanded Analogy between Boltzmann Kinetic Theory of Fluids and Turbulence," *Journal of Fluid Mechanics*, Vol. 519, 2004, pp. 301–314.

[32] Chen, H., Teixeira, C., and Molvig, K., "Realization of Fluid Boundary Conditions via Discrete Boltzmann Dynamics," *Int. J. Mod. Phys. C*, Vol. 09, No. 08, 1998, pp. 1281–1292.

[33] Launder, B. E., and Spalding, D. B., "The Numerical Computation of Turbulent Flows," *Numerical Prediction of Flow, Heat Transfer, Turbulence and Combustion*, edited by S. V. Patankar, A. Pollard, A. K. Singhal, and S. P. Vanka, Pergamon, 1983, pp. 96–116.

[34] Williams, J. E. F., and Hawkings, D. L. H. R., “Sound Generation by Turbulence and Surfaces in Arbitrary Motion,” *Philosophical Transactions of the Royal Society of London. Series A, Mathematical and Physical Sciences*, Vol. 264, No. 1151, 1969, pp. 321–342.

[35] Farassat, F., and Succi, G. P., “A Review of Propeller Discrete Frequency Noise Prediction Technology with Emphasis on Two Current Methods for Time Domain Calculations,” *Journal of Sound and Vibration*, Vol. 71, No. 3, 1980, pp. 399–419.

[36] Casalino, D., “An Advanced Time Approach for Acoustic Analogy Predictions,” *Journal of Sound and Vibration*, Vol. 261, No. 4, 2003, pp. 583–612.

[37] Merino-Martínez, R., Sijtsma, P., Snellen, M., Ahlefeldt, T., Antoni, J., Bahr, C., Blacodon, D., Ernst, D., Finez, A., Funke, S., et al., “A review of acoustic imaging methods using phased microphone arrays,” *CEAS Aeronautical Journal*, Vol. 10, No. 1, 2019, pp. 197–230.

[38] Brooks, T. F., and Humphreys, W. M., “A deconvolution approach for the mapping of acoustic sources (DAMAS) determined from phased microphone arrays,” *Journal of Sound and Vibration*, Vol. 294, No. 4, 2006, pp. 856–879.

[39] Sarradj, E., “A fast signal subspace approach for the determination of absolute levels from phased microphone array measurements,” *Journal of Sound and Vibration*, Vol. 329, No. 9, 2010, pp. 1553–1569.

[40] Arcondoulis, E. J., Liu, Y., Xu, P., Li, Q., Wei, R., Yang, Y., and Chen, N., “Experimentally Based CLEAN-SC Array Pairing Method for Distributed Aeroacoustic Sources,” *AIAA Journal*, Vol. 60, No. 4, 2022, pp. 2678–2684.

[41] Arcondoulis, E. J., Liu, Y., Xu, P., and Chen, N., “An array pairing method for localizing distributed sources by acoustic beamforming,” *The Journal of the Acoustical Society of America*, Vol. 147, No. 1, 2020, pp. EL7–EL12.

[42] Zamponi, R., Moreau, S., and Schram, C., “Rapid distortion theory of turbulent flow around a porous cylinder,” *Journal of Fluid Mechanics*, Vol. 915, 2021.

[43] Batchelor, G. K., *An introduction to fluid dynamics*, Cambridge university press, 1967.